The spin-gap state and the linear-chain state in δ-phase $Ag_xV_2O_5$ with a double-layered structure

2001 J. Phys.: Condens. Matter 13 10399

(http://iopscience.iop.org/0953-8984/13/46/311)

INSTITUTE OF PHYSICS PUBLISHING JOURNAL OF PHYSICS: CONDENSED MATTER

J. Phys.: Condens. Matter **13** (2001) 10399–10416 PII: S0953-8984(01)24858-9

The spin-gap state and the linear-chain state in δ-phase $Ag_xV_2O_5$ with a double-layered structure

Masashige Onoda and Ryuichi Arai

Institute of Physics, University of Tsukuba, Tennodai, Tsukuba 305-8571, Japan

Received 16 May 2001, in final form 17 July 2001
Published 2 November 2001
Online at stacks.iop.org/JPhysCM/13/10399

Abstract

The crystal structure and electronic properties of the δ-phase $Ag_xV_2O_5$ system, where $0.65 \leqslant x \leqslant 0.90$, have been explored by means of x-ray four-circle diffraction and through measurements of lattice constants, electrical resistivity, thermoelectric power, magnetization and electron paramagnetic resonance. The structure of $Ag_{0.68}V_2O_5$ has been redetermined with residual factors of $R = 0.054$ and $R_w = 0.051$. It is built up of V_2O_5 double layers and Ag ions located at two disordered sites between the layers. The δ-$Ag_xV_2O_5$ system is characterized against the composition as follows. For the range $0.65 \leqslant x \leqslant 0.75$, first-order phase transitions with structural, transport and magnetic anomalies appear at $T_{c1} \simeq 220$ K, below which, accompanied with significant reduction of the superexchange coupling constants, a nearly $\frac{1}{6}$-filled compound has a spin gap originating from the trellis-layer model and other compositions probably remain paramagnetic with susceptibility maxima. For $0.80 \leqslant x < 0.85$, the only transport anomaly occurs at $T_{c2} \simeq 170$ K, to which the crossover point is $x_c \simeq 0.775$, and for $0.85 \leqslant x \leqslant 0.90$, no anomaly exists there. The magnetic properties for $0.80 \leqslant x \leqslant 0.90$ essentially exhibit linear-chain behaviours. The transport properties for $x \leqslant x_c$ and $x > x_c$ are understood as indicating the hopping conductions of negative and positive small polarons, respectively.

S This article has associated online supplementary data files

1. Introduction

Generally, transition-metal (TM) oxides have crystal structures formed by the linkage of rigid units such as octahedra, pyramids or tetrahedra of oxygens. Electrons located in the TM–O bands contribute to the physical properties. Various TM oxides with unfilled d orbitals have been investigated intensively in order to clarify the properties of correlated-electron, electron–phonon-coupling and quantum spin-fluctuation systems.

Recent works on the spin-fluctuation and frustration effects in the low-dimensional system based on vanadium oxides have been performed for systems such as a half-filled insulator

CaV_nO_{2n+1} with $n = 2$–4. This system consists of V_nO_{2n+1} layers formed by sharing edges and corners of VO_5 pyramids, where Ca atoms are situated between the layers, and it has a two-dimensional $S = \frac{1}{2}$ configuration at the V^{4+} site of the $\frac{1}{n+1}$-depleted square lattice [1–3]. CaV_4O_9 exhibits a singlet ground state originating from weakly coupled metaplaquettes [4, 5], and CaV_2O_5 also indicates a singlet state essentially due to the corner-sharing dimerization [3, 6]. On the other hand, CaV_3O_7 has a stripe-phase magnetic order [7].

Quarter-filled NaV_2O_5 has a similar structure to that of CaV_2O_5 [3, 8–10]. This compound is an insulator and shows one-dimensional $S = \frac{1}{2}$ magnetic properties with spins attached to a V–O–V molecular orbital [8, 11]. A spin-singlet transition appears at $T_c = 34$ K with a lattice distortion [12]. One of the authors has explored the crossover between the spin-gap and the linear-chain properties as a function of electron concentration through the $Ca_{1-x}Na_xV_2O_5$ system [13]. The magnetic properties for $0 < x \leqslant 0.1$ have been interpreted as being governed by contributions from the dimer and from the isolated spins that are present due to the breaking of the dimer. On the other hand, the properties for $0.9 \leqslant x < 1$ still exhibit linear-chain behaviours, and for $x \leqslant 0.97$, the singlet transition disappears, and no magnetic ordering takes place. It is difficult to clarify whether the crossover between the dimer state and the linear-chain state is continuous or not, since the compounds with $0.1 < x < 0.8$ are not obtained.

In the vanadium bronze system with the chemical formula $M_xV_2O_5$, where M denotes alkali, alkaline-earth or other metal, and $0 < x < 1$, a tunnel or a layered structure appears depending on x and the ionic radius of M [14]. Thus, the electronic properties are expected to become low dimensional [15]. The number of electrons donated by M may be controlled as a function of x. The subject of this work is the δ-phase of $Ag_xV_2O_5$, which was originally synthesized under hydrothermal conditions [16]. The δ-phase compounds prepared at 923 K have Ag concentrations ranging from 0.69 to 0.85 [17]. The structural model for $x = 0.68$ is expressed as V_2O_5 double layers and Ag ions located between the layers [16]. The transport properties for sintered specimens of δ-$Ag_xV_2O_5$ indicate this system to be nonmetals and to have anomalies at $T_c = 235$, 230 and 215 K for $x = 0.72$, 0.75 and 0.80, respectively [18, 19]. The magnetic measurements reveal that the susceptibility at temperatures above T_c follows the Curie–Weiss law, and below T_c, it becomes smaller than the value expected from the high-temperature behaviour. The underlying physical mechanisms for these results are not clear. This system has recently been proposed for use as the positive electrode for lithium secondary cells [20].

Against the background described above, the crystal structure and electronic properties of the δ-$Ag_xV_2O_5$ system, where $0.65 \leqslant x \leqslant 0.90$, have been investigated in detail by means of x-ray four-circle diffraction and through measurements of lattice constants, electrical resistivity, thermoelectric power, magnetization and electron paramagnetic resonance (EPR). The lattice constants as functions of x and temperature, and the crystal structure redetermined in order to estimate the precise valence distribution are described in section 2. Detailed composition dependences of electronic properties for sintered specimens as well as crystalline ones are also discussed in section 3. Section 4 is devoted to further discussion and conclusions.

2. Crystal structure

2.1. Sample preparation, chemical analysis and lattice constants

Sintered specimens of $Ag_xV_2O_5$ with the nominal range $0.60 \leqslant x \leqslant 0.95$ were prepared by the solid-state reaction method as follows. Mixtures of $\frac{x}{2}Ag_2O$ (99.9% purity), $(1 - \frac{x}{4})V_2O_5$ (99.99% purity) and $\frac{x}{4}V_2O_3$ that was made according to the procedure described in reference [21] were ground and pressed into pellets. These were sealed in quartz tubes with Ar and

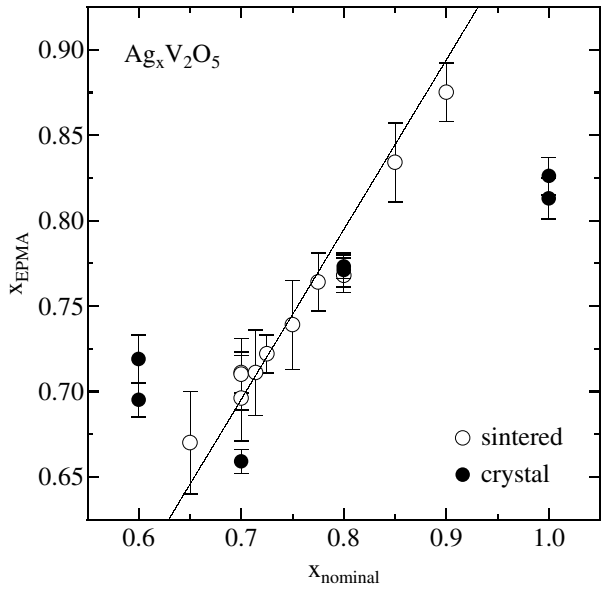

Figure 1. The relation between the nominal Ag concentration x_{nominal} and the EPMA value x_{EPMA} for the sintered specimens and the crystalline ones of δ-$Ag_xV_2O_5$, where the full line indicates their linear relation for the sintered specimens.

then heated at 993 K for 12 hours. The single crystals of $Ag_xV_2O_5$ were also prepared by the Bridgman method at 1023–1048 K with the use of the above mixtures. For the prepared specimens, an electron-probe microanalysis (EPMA) and an x-ray powder diffraction investigation were performed at room temperatures using a JEOL JXA-8621 and a Rigaku RAD-IIC diffractometer with Cu Kα radiation, respectively.

For the sintered and single-crystal specimens with the nominal compositions in the range $0.65 \leqslant x \leqslant 0.90$, the single phase was confirmed. For $x = 0.60$ and 0.95, impurity phases of β-phase $Ag_xV_2O_5$ and Ag metal appeared, respectively, so these two compounds are excluded below. The Ag concentration estimated by EPMA, x_{EPMA}, is plotted in figure 1 as a function of the nominal concentration x_{nominal}. For the sintered specimens, x_{EPMA} is described as $x_{\mathrm{EPMA}} = (0.991 \pm 0.006)x_{\mathrm{nominal}}$ as shown by the full line. Thus, it may be concluded that the actual concentration of Ag agrees with the nominal value within an error. On the other hand, for the single-crystal specimens, x_{EPMA} is significantly different from x_{nominal} owing to the inhomogeneous solidification accompanied with impurity phases, β-$Ag_xV_2O_5$ and $AgVO_3$. We shall use the nominal and EPMA compositions as those of the sintered and single-crystal specimens, respectively.

Figures 2(a)–2(e) show the x-dependences of the lattice constants at room temperature, obtained from the comparison with the powder diffraction pattern calculated on the basis of the atomic parameters of $Ag_{0.68}V_2O_5$ which will be described in section 2.2. The results determined by an x-ray four-circle diffraction are also plotted as the full circles. The lattice constant of the a-axis increases monotonically and that of the c-axis decreases in a similar manner with increasing x. The results for the b-axis and β (figures 2(b) and 2(d)) do not show monotonic dependence on the composition, but seem to have a boundary at $x_{\mathrm{c}} \simeq 0.775$. The temperature dependences of the lattice constants for $x = 0.65$ and 0.775 in the heating process are shown in figures 3(a)–3(e). For $x = 0.65$, abrupt change in the lattice constants appears at $T_{\mathrm{c1}} \simeq 220$ K, but it does not appear for $x = 0.775$. As will be described in section 3, the

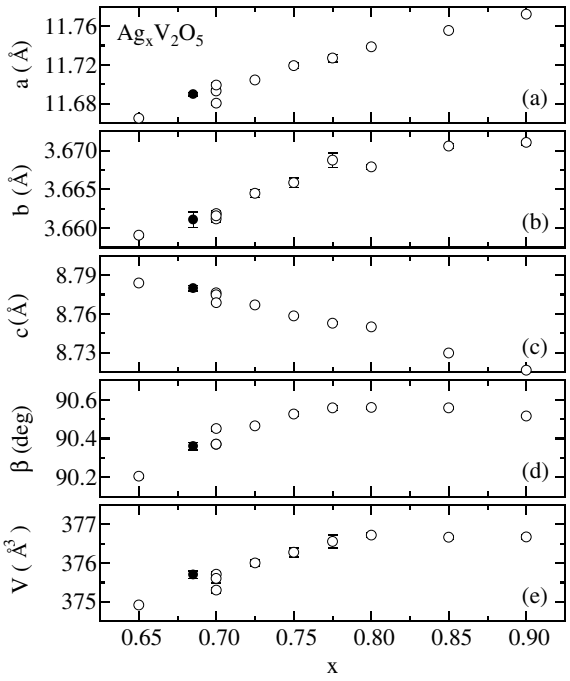

Figure 2. The composition dependences of the lattice constants of δ-$Ag_xV_2O_5$ at room temperature, where the open and full circles indicate results for the sintered specimens and those determined from the x-ray four-circle diffraction, respectively.

transport and magnetic properties change significantly at x_c and $x \simeq 0.85$, and those with $x < x_c$ exhibit first-order transitions at T_{c1}.

2.2. Structure determination

The x-ray four-circle diffraction measurements were carried out on a Rigaku AFC-7R diffractometer (custom-made) and a DI-XRD CAD4 with graphite-monochromated Mo Kα radiation at 293 K. The single crystal with dimensions of $0.14 \times 0.06 \times 0.01$ mm made by the solid-state reaction method with the nominal composition $x = 0.70$ was mounted on a glass fibre. Consideration of the reflections indicated that the crystal is (0 0 1) twinned for the lattice constants described below. Then, each setting parameter was determined precisely, so that only reflections from the single domain were obtained. The intensity data were collected over a maximum 2θ range of 90° using the ω–2θ scan technique. Of 1665 unique reflections from the single domain with removal of the overlapped reflections due to the twinning, 946 reflections with $|F_o| \geqslant 3\sigma$, F_o and σ being an observed structure factor and its standard deviation, respectively, were used. Lorentz polarization, the absorption correction and the secondary extinction correction were applied, where the transmission factors were in the range 0.42–0.80. The internal consistency of the reflections was estimated on the basis of F_o^2 to be $R_{int} = 0.073$.

Through the systematic absences of reflections, a statistical analysis of the intensity distribution and the successful solution and refinement of the structure, the crystal data were determined to be: monoclinic with space group $C2/m$ (No 12); $a = 11.690(2)$ Å, $b = 3.661(1)$ Å, $c = 8.780(2)$ Å, $\beta = 90.36(2)°$, $V = 375.7(1)$ Å^3, $Z = 4$; μ(Mo Kα) $= 8.312$ mm^{-1}; and

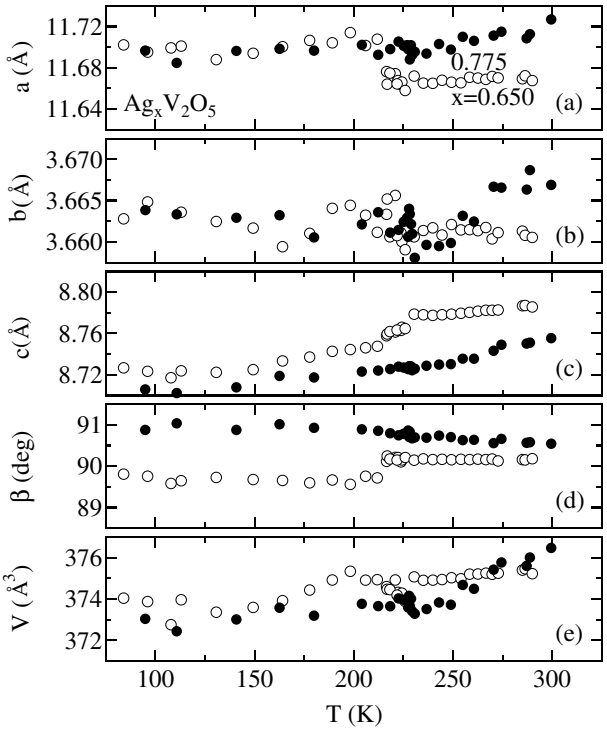

Figure 3. The temperature dependences of the lattice constants of δ-$Ag_xV_2O_5$ with $x = 0.65$ and 0.775 in the heating process.

$D_{cal} = 4.520$ Mg m^{-3}. These lattice constants are similar to those reported previously, except for that of the *a*-axis.

The structure was solved by direct methods [22], expanded using Fourier techniques and refined by full-matrix least-squares calculations with anisotropic displacement parameters. The atomic scattering factors were taken from reference [23], and anomalous dispersion effects were included with the values given by reference [24]. The residual factors defined as

$$R = \left[\sum(|F_o| - |F_c|)^2\right] \Big/ \left(\sum |F_o|\right) \tag{1}$$

and

$$R_w = \left\{\left[\sum w(|F_o| - |F_c|)^2\right] \Big/ \left(\sum w F_o^2\right)\right\}^{1/2} \tag{2}$$

where $|F_c|$ is a calculated structure factor, are finally[1] $R = 0.054$ and $R_w = 0.051$. All of the calculations were performed using the teXsan crystallographic software package [25].

The atomic coordinates, equivalent isotropic thermal parameters and anisotropic displacement parameters are listed in table 1. Selected interatomic distances and angles are listed in table 2. The atomic coordinates except those for Ag determined here are roughly consistent with the previous result [16], but significant deviations of over 1×10^{-2} exist for oxygen atoms O4 and O5. Thus, the interatomic distances for these atoms are significantly different from those presented previously. Moreover, standard

[1] Supplementary data files are available from the article's abstract page in the online journal; see http://www.iop.org.

Table 1. Atomic coordinates, equivalent isotropic thermal parameters B_{eq} (Å^2) and anisotropic displacement parameters U_{ij} of δ-$Ag_{0.68}V_2O_5$ at 293 K, where $y = 0$ and $U_{12} = U_{23} = 0$ for all of the atoms. B_{eq} and U_{ij} are defined by $B_{eq} = \frac{8}{3}\pi^2[U_{11}(aa^*)^2 + U_{22}(bb^*)^2 + U_{33}(cc^*)^2 + 2U_{12}aa^*bb^* \cos\gamma + 2U_{13}aa^*cc^* \cos\beta + 2U_{23}bb^*cc^* \cos\alpha]$, and the parameters are defined in the thermal factor form $T = \exp[-2\pi^2(a^{*2}U_{11}h^2 + b^{*2}U_{22}k^2 + c^{*2}U_{33}l^2 + 2a^*b^*U_{12}hk + 2a^*c^*U_{13}hl + 2b^*c^*U_{23}kl)]$. The occupancy probabilities for Ag1 and Ag2 are 0.442(3) and 0.242(3), respectively.

Atom	x	z	B_{eq}	U_{11}	U_{22}	U_{33}	U_{13}
Ag1	0.6211(2)	0.0210(3)	2.27(4)	0.043(1)	0.0207(8)	0.0220(7)	−0.0026(8)
Ag2	0.5699(4)	0.0305(5)	2.61(7)	0.065(3)	0.011(1)	0.023(1)	0.011(2)
V1	0.2301(1)	0.3351(1)	0.86(2)	0.0102(5)	0.0084(4)	0.0140(4)	−0.0005(3)
V2	0.93367(10)	0.3343(1)	0.78(2)	0.0087(4)	0.0080(4)	0.0128(4)	0.0009(3)
O1	0.0800(4)	0.3977(6)	1.07(8)	0.012(2)	0.013(2)	0.015(2)	0.000(2)
O2	0.7600(4)	0.3823(6)	1.05(8)	0.012(2)	0.009(2)	0.019(2)	0.002(2)
O3	0.3993(4)	0.3607(6)	1.08(8)	0.011(2)	0.012(2)	0.018(2)	−0.002(2)
O4	0.9484(5)	0.1492(6)	1.40(9)	0.020(3)	0.019(2)	0.015(2)	0.003(2)
O5	0.2099(5)	0.1530(6)	1.60(9)	0.016(2)	0.028(3)	0.016(2)	−0.003(2)

Table 2. Selected interatomic distances (Å) and angles (deg) of δ-$Ag_{0.68}V_2O_5$ at 293 K, where the translation codes are (i) x, y, z; (ii) $-\frac{1}{2} + x, -\frac{1}{2} + y, z$; (iii) $-\frac{1}{2} + x, \frac{1}{2} + y, z$; (iv) $1-x, -y, 1-z$; (v) $1+x, y, z$; (vi) $\frac{1}{2}+x, \frac{1}{2}+y, z$; (vii) $\frac{1}{2}+x, -\frac{1}{2}+y, z$; (viii) $\frac{3}{2} - x, \frac{1}{2}-y, -z$; (ix) $\frac{3}{2} - x, -\frac{1}{2} - y, -z$; (x) $1 - x, -y, -z$; (xi) $\frac{1}{2} - x, \frac{1}{2} - y, 1 - z$; (xii) $\frac{1}{2} - x, -\frac{1}{2} - y, 1 - z$; (xiii) $2 - x, -y, 1 - z$; (xiv) $-1 + x, y, z$.

V–O polyhedra		Ag–O polyhedra		V–V, Ag–Ag and V–O–V	
$V1O_6$		$Ag1O_7$ or $Ag1O_5$		V1(i)–V1(xi, xii)	3.454(2)
V1(i)–O1(i)	1.842(5)	Ag1(i)–O4(ii, iii)	2.953(5)	V2(i)–V2(xiii)	3.289(2)
V1(i)–O2(ii, iii)	1.909(2)	Ag1(i)–O4(viii, ix)	2.496(4)	V1(i)–V2(ii, iii)	3.002(1)
V1(i)–O2(iv)	2.483(5)	Ag1(i)–O5(vi, vii)	2.399(4)	V1(i)–V2(iv)	3.487(2)
V1(i)–O3(i)	1.990(5)	Ag1(i)–O5(x)	2.504(6)	V1(i)–V2(xiv)	3.465(2)
V1(i)–O5(i)	1.615(5)			Ag1(i)–Ag1(x)	2.853(5)
				Ag1(i)–Ag2(i)	0.605(5)
$V2O_6$		$Ag2O_7$ or $Ag2O_6$		Ag1(i)–Ag2(x)	2.276(6)
V2(i)–O1(iv)	2.360(5)	Ag2(i)–O4(ii, iii)	2.544(5)	Ag2(i)–Ag2(x)	1.72(1)
V2(i)–O1(v)	1.796(5)	Ag2(i)–O4(viii, ix)	2.425(4)	V1(vi)–O2(i)–V1(vii)	147.1(3)
V2(i)–O2(i)	2.076(5)	Ag2(i)–O5(vi, vii)	2.676(6)	V2(ii)–O3(i)–V2(iii)	151.5(3)
V2(i)–O3(vi, vii)	1.889(2)	Ag2(i)–O5(x)	3.045(7)	V1(i)–O1(i)–V2(xiv)	144.6(3)
V2(i)–O4(i)	1.635(5)			V1(i)–O3(i)–V2(ii)	101.4(2)
				V1(vi)–O2(i)–V2(i)	97.7(2)

deviations in this work are greatly improved. Figures 4(a) and 4(b) show the crystal structures projected on the *ab*- and *ac*-planes with the polyhedral scheme, respectively. There are two independent vanadium atoms labelled V1 and V2. The V1–O and V2–O bond lengths range from 1.615 to 2.483 Å and from 1.635 to 2.360 Å, respectively, indicating that each V atom forms a distorted octahedron. The short bonds of 1.615 and 1.635 Å correspond to the double bond V=O . The structure is described in terms of the $V1O_6$ and $V2O_6$ octahedra which are joined by sharing edges and corners to form double layers of V_2O_5. This kind of layered structure is common to the δ-phase of $M_xV_2O_5$ with M = K and Sr [14].

On the basis of the bond-length–bond-strength relation [26], the effective valences at the V1 and V2 sites are estimated to be 4.61 and 4.65, respectively, indicating that the valence distribution of V ions is almost homogeneous. The ground-state wavefunctions for the $V1O_6$

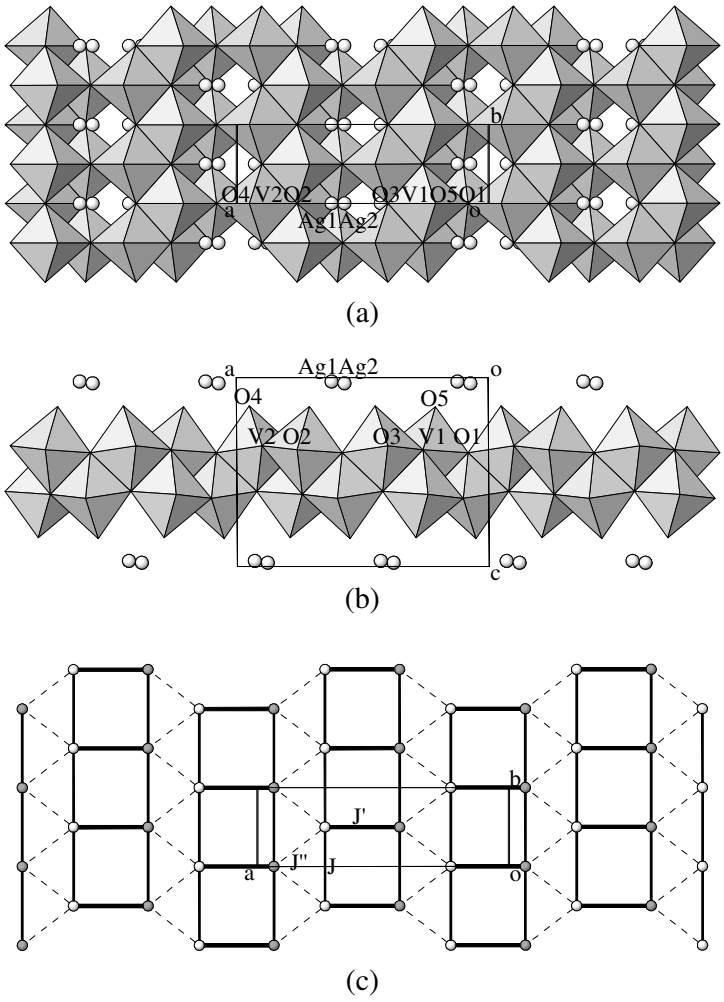

Figure 4. The crystal structures of δ-$Ag_{0.68}V_2O_5$ at 293 K: the projections on (a) the *ab*-plane and (b) the *ac*-plane with the polyhedral scheme; and (c) the simplified spin network, where the thick lines and the broken lines denote the corner-sharing V–V paths (J and J') and the edge-sharing one (J'') for the exchange couplings, respectively.

and $V2O_6$ octahedra are found to be composed of, respectively, $0.899d_{xy} - 0.438d_{yz}$ and $0.922d_{xy} + 0.388d_{yz}$, where $\boldsymbol{x} \parallel \boldsymbol{a}$ and $\boldsymbol{y} \parallel \boldsymbol{b}$, with the use of the Hartree–Fock function for V^{4+} [27]. The effective valences of the oxygen atoms at the O1–O5 sites are given as 2.00, 1.90, 2.00, 1.63 and 1.73, respectively. Due to the V=O bond, the hole densities at the O4 and O5 sites are significantly large.

The Ag atoms have two disordered sites labelled Ag1 and Ag2 with respective occupancy probabilities of 0.442(3) and 0.242(3), which is different from the previous result [16]. These probabilities lead to the chemical formula of $Ag_{0.68}V_2O_5$. Due to the strong Coulomb repulsion, the Ag1 and Ag2 sites with interatomic distances smaller than 2.276 Å cannot be occupied simultaneously. Both sites are located between the V_2O_5 layers. The Ag ions at the Ag1 and Ag2 sites are surrounded with five and six O atoms, respectively, on the assumption of a coordination sphere of 2.70 Å. The Ag1–O and Ag2–O bond lengths range from 2.399 to

2.504 Å and from 2.425 to 2.676 Å, respectively, such that their average values are 2.459 and 2.548 Å. Thus, the ionic radii for the Ag1 and Ag2 sites are estimated to be 1.079 and 1.168 Å, which agree well with those for five and six coordinations of Ag^+ ion [28].

3. Electronic properties

3.1. Electrical resistivity

The four-terminal electrical resistivities for the sintered specimens, ρ_s, and for the direction perpendicular to the $\boldsymbol{c}^*$-axis of the crystalline ones, $\rho_{\perp c^*}$, of $Ag_xV_2O_5$ were measured by a dc method in the temperature region between 80 and 300 K.

The resistivities ρ_s and $\rho_{\perp c^*}$ as a function of the inverse temperature are shown in figures 5(a) and 5(b), respectively. Here, the open and full symbols indicate results for the cooling and heating processes, respectively. The resistivities for the sintered specimens are larger than those for the crystalline ones, which is partly attributable to granular texture effects of the specimens. It can also be explained on the basis of the crystal structure; that is, the resistivity in the V_2O_5 layer is expected to be smaller than that along the $\boldsymbol{c}^*$-axis. For all of the specimens, ρ increases with decreasing temperature. There are significant anomalies at $T_{c1} \simeq 220$ K with a rapid increase of the resistivity for the range $0.65 \leqslant x \leqslant 0.75$. For $x_c \simeq 0.775 \leqslant x \leqslant 0.85$, slight anomalies appear at $T_{c2} \simeq 170$ K as compared with those for $0.65 \leqslant x \leqslant 0.75$. For the sintered specimens and the crystalline ones, the temperatures $T_{c\rho}$ (T_{c1} and T_{c2}) at which $|\mathrm{d} \ln \rho / \mathrm{d}T^{-1}|$ has a peak against x are plotted in figure 6 as the circles and squares, respectively, where the full (open) symbols indicate results for the heating (cooling) process. Since the temperatures $T_{c\rho}$ for the heating and cooling processes are different, the transition is of first order. For the sintered specimen with $x = 0.90$, no significant anomaly exists there, although the resistivity seems to have a large thermal hysteresis.

From the full lines at high temperatures in figures 5(a) and 5(b), the energy gaps E_ρ defined by

$$\rho_i = \rho_0 \exp(E_\rho / T) \tag{3}$$

where $i = s$ and $\perp c^*$, and ρ_0 is assumed to be a constant, range from 1200 to 1600 K for the sintered specimens and from 900 to 1100 K for the crystalline ones. Here, their composition dependence is not significant. The reason that E_ρ for the crystalline specimens is smaller than that for the sintered specimens may be the same as that described for the difference of their resistivities.

3.2. Thermoelectric power

The thermoelectric powers for the sintered specimens, S_s, and for the direction perpendicular to the $\boldsymbol{c}^*$-axis for the crystalline ones, $S_{\perp c^*}$, of $Ag_xV_2O_5$ were measured by a dc method at temperatures from 80 to 300 K.

Figures 7(a) and 7(b) show S_s and $S_{\perp c^*}$ against the inverse temperature, respectively. In these figures, the open and full symbols indicate results for the cooling and heating processes, respectively. At high temperatures, the thermoelectric powers for $0.65 \leqslant x < 0.75$ are negative, suggesting electron carrier conduction, and those for $x \geqslant 0.75$ are positive, which is indicative of hole conduction. All of the data basically exhibit semiconducting behaviours, which is consistent with the resistivity result. There exist first-order anomalies at $T_{c1} \simeq 220$ K with a hollow or hump for the range $0.65 \leqslant x \leqslant 0.773$ ($\simeq x_c$) in spite of their crystallinity. For 0.771 ($\simeq x_c$) $\leqslant x \leqslant 0.826$, there are similar anomalies at $T_{c2} \simeq 170$ K. The composition with $x = 0.826$ exhibits a rather broad transition and those with $x = 0.85$ and 0.90 do not indicate

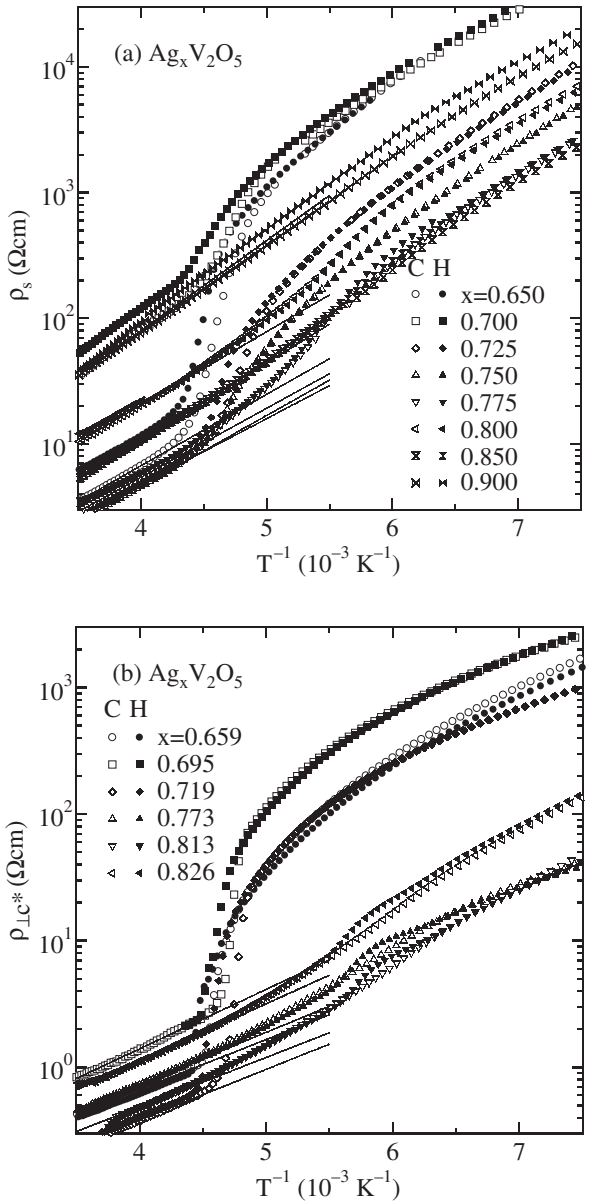

Figure 5. The temperatures dependences of the electrical resistivities for (a) the sintered specimens, ρ_s, and (b) the crystalline ones, $\rho_{\perp c^*}$, of δ-$Ag_xV_2O_5$ in the cooling 'C' and heating 'H' processes, where the full lines in (a) and (b) show fits to equation (3).

any sign of transitions. For the sintered specimens and the crystalline ones, the temperatures T_{cS} (T_{c1} and T_{c2}) at which $|dS/dT^{-1}|$ has a peak are summarized as a function of x in figure 6 by the diamonds and triangles, respectively, where the full (open) symbols indicate results for the heating (cooling) process. In addition, the compositions with $x = 0.75$ and 0.80 have another anomaly at $T_{c3} \simeq 230$ K.

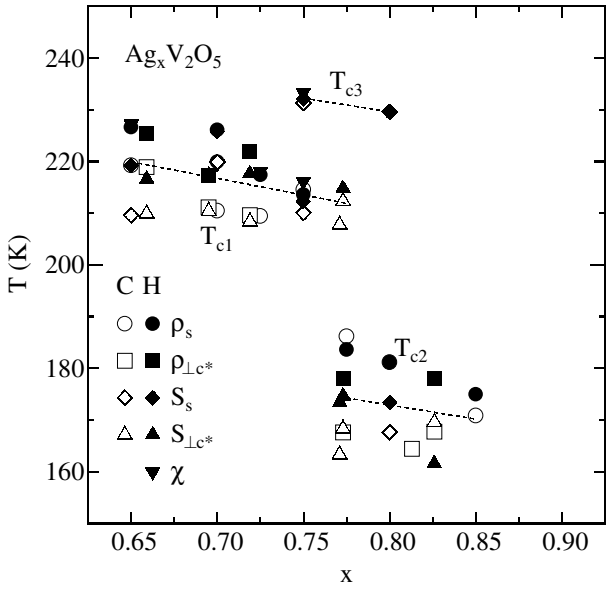

Figure 6. The composition dependence of the electronic transition temperatures, T_{c1}, T_{c2} and T_{c3}, of δ-$Ag_xV_2O_5$, estimated from the data on the electrical resistivity (ρ_s and $\rho_{\perp c^*}$), the thermoelectric power (S_s and $S_{\perp c^*}$) and the magnetic susceptibility (χ) in the cooling 'C' and heating 'H' processes, where the dotted lines are drawn as guides to the eye.

On the basis of the full lines at high temperatures in figures 7(a) and 7(b), the temperature-independent value S_0 and the apparent gap E_S, empirically defined by

$$S_i = eE_S/T + S_0 \tag{4}$$

where $i =$ s and $\perp c^*$, are plotted against x in figures 8(a) and 8(b), respectively. For the range $0.65 \leqslant x \leqslant x_c$, $|S_0|$ decreases linearly with increase of x, and E_S is roughly constant close to zero. This suggests that the electron transport in this composition range is regarded as being the hopping of small polarons due to electrostatic potentials at the V sites that are near neighbours to Ag^+ or a variable-range hopping due to the random-potential effect of Ag^+ [29, 30]. Here, let us consider the thermoelectric power following the former model, where all of mobile charge carriers are created and the fraction of V sites occupied by them is fixed. In this case, E_ρ for the electrical resistivity is the hopping energy of small polarons, and S_0 corresponds to the so-called Heikes formula [31]:

$$S_p = \frac{k}{e} \ln\left(\frac{x}{2-x}\right) + S_0' \tag{5}$$

where k is the Boltzmann coefficient and S_0' is a constant depending on another scattering mechanism. This formula qualitatively accounts for the x-dependence of S_0 for the range $0.65 \leqslant x \leqslant x_c$ as shown by the full curve in figure 8(a) with $S_0' = 24\,\mu\mathrm{V\,K^{-1}}$. In order to estimate the hopping energy of a polaron precisely, a small temperature dependence of the pre-exponential term ρ_0 in equation (3) should be considered. However, this is difficult, since the high-temperature region in which the measurements are made is narrow as compared with the magnitude of E_ρ.

The result for $x > x_c$, especially for $x = 0.85$ and 0.90 without transitions, indicates that the difference between E_ρ and E_S becomes small, but the small-polaron model may be still

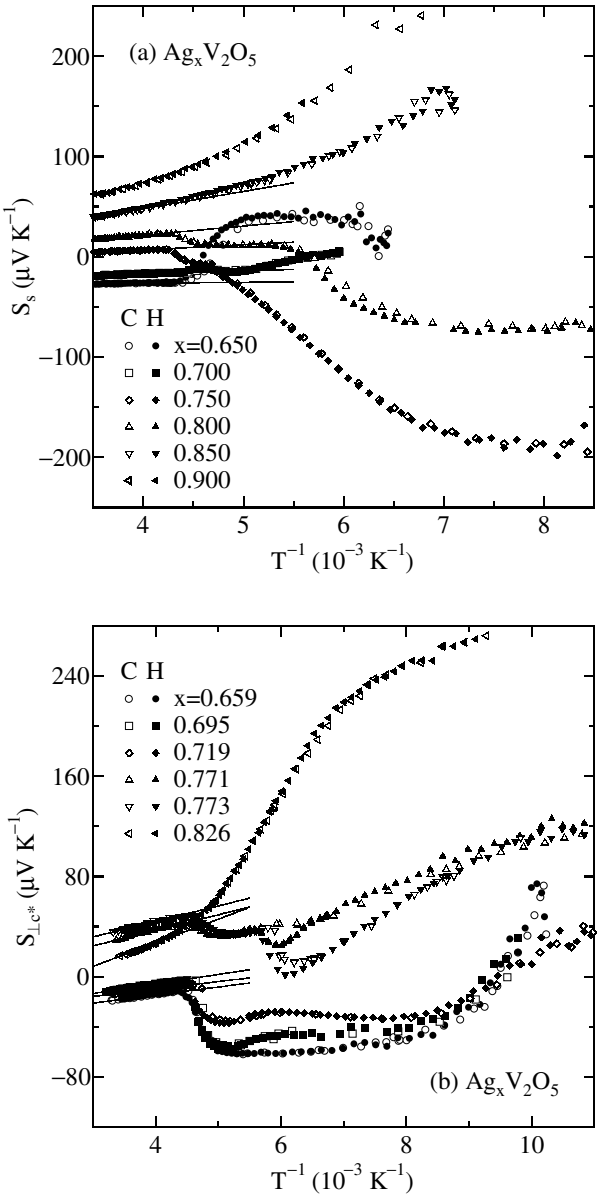

Figure 7. The temperature dependences of the thermoelectric powers for (a) the sintered specimens, S_s, and (b) the crystalline ones, $S_{\perp c^*}$, of δ-$Ag_xV_2O_5$ in the cooling 'C' and heating 'H' processes, where the full lines in (a) and (b) indicate fits to equation (4).

valid with a temperature-dependent carrier fraction. Thus, E_S is the trapping energy of the hole, and the difference between E_ρ and E_S may correspond to the motional enthalpy of the polaron. It should be noted that the change of the transport mechanisms with the increase of x is similar to that on the insulator side in the spinel-type $Li_xMg_{1-x}V_2O_4$ system with a metal–insulator transition [29]. Here, MgV_2O_4 is a Mott-type polaronic insulator, and hole

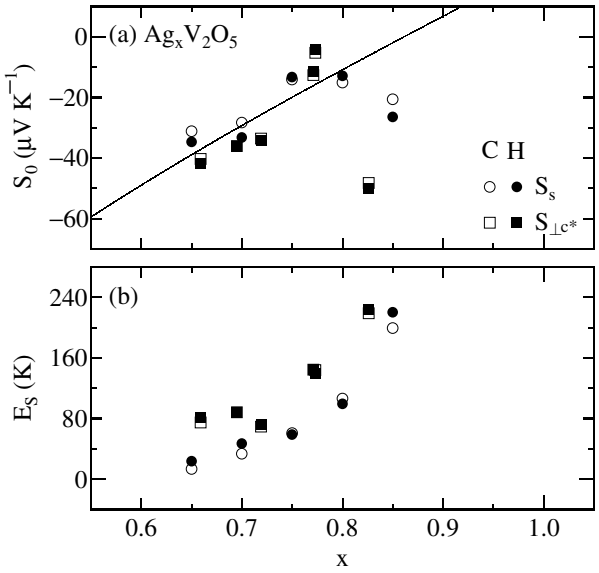

Figure 8. The composition dependences of the parameters in equation (4); (a) S_0 and (b) E_S, estimated from the data on the thermoelectric power (S_s and $S_{\perp c^*}$) of δ-$Ag_xV_2O_5$ in the cooling 'C' and heating 'H' processes, where the full curve in (a) shows a fit to equation (5).

carriers introduced by the substitution of Li for Mg lead to the variable-range hopping-type phase in the region $0 < x < 0.4$.

3.3. Magnetization

The magnetizations of the sintered specimens of $Ag_xV_2O_5$ were measured by the Faraday method with a field of up to 1 T at temperatures between 4.2 and 900 K. Here, both cooling and heating processes were examined at temperatures above 300 K, and below it, only the heating process was performed. The magnetic susceptibility χ was deduced from the linear part of the magnetization–field (M–H) curve with decreasing field.

The temperature dependence of χ^{-1} is shown in figure 9(a) and the low-temperature part of χ is indicated in figure 9(b). For all of the specimens, χ at temperatures above 300 K is reversible for the cooling and heating processes, and it is well explained by considering the contributions of the Curie–Weiss-type susceptibility χ_{CW} and the temperature-independent susceptibility of the Van Vleck orbital and diamagnetic components, χ_0:

$$\chi = \chi_{CW} + \chi_0 \tag{6}$$

$$\chi_{CW} = \frac{C}{T + T_W} \tag{7}$$

where C and T_W are the Curie constant and the Weiss temperature, respectively. The full curves in figure 9(a) are drawn on the basis of the parameters listed in table 3. Since the V^{4+} ions for $x = 0.65$, 0.70 and 0.90 have the average g-factor of 1.96 as will be described in section 3.4, the Curie constants listed here are consistent with the values expected from a model where the Ag doping with x gives rise to an unpaired electron with $x/2$ per V ion. As found in table 3, T_W decreases with increasing x. In contrast, in the molecular field approximation, T_W is expected to be proportional to x^2. Therefore, in this system, the local network for the spin–spin interaction may change with x. In effect, the lattice constants parallel to the V_2O_5

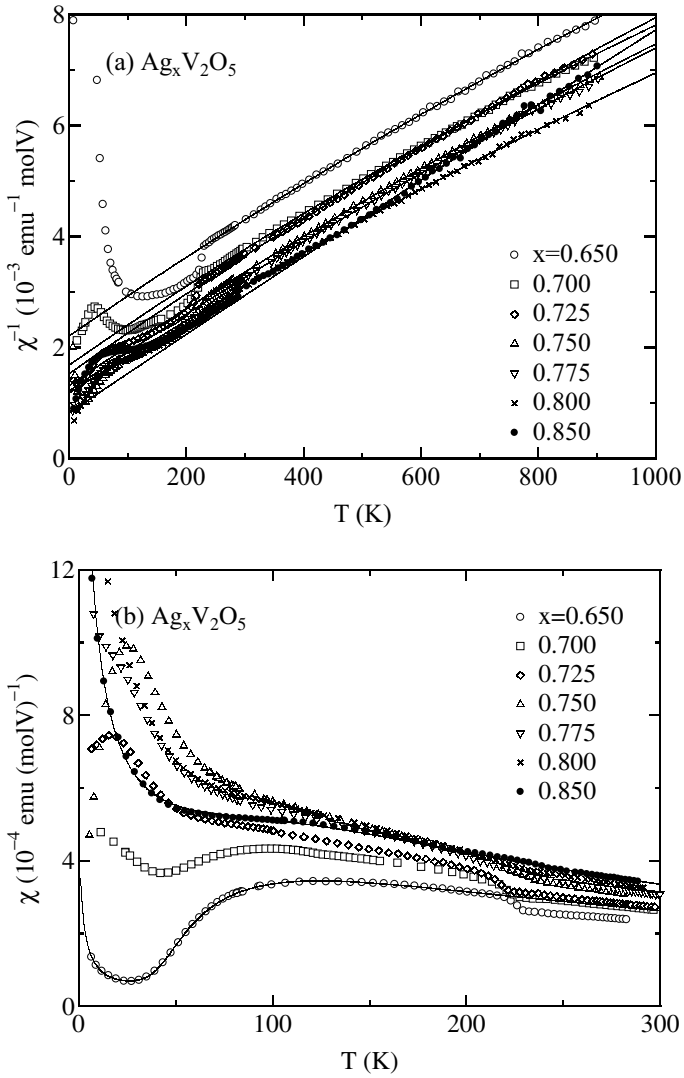

Figure 9. The temperature dependences of (a) the inverse of the magnetic susceptibility χ^{-1} and (b) χ at low temperatures for δ-$Ag_xV_2O_5$ in the heating process, where the full curves in (a) are drawn on the basis of equation (6), and those for $x = 0.65$ and 0.85 in (b) are results obtained with equations (8) and (9), respectively.

layer increase with x as shown in figures 2(a) and 2(b), possibly leading to the reduction of the exchange coupling constants.

At temperatures below 300 K, deviations from the Curie–Weiss law are significant for all of the specimens. For $0.65 \leqslant x \leqslant 0.75$, a jump of χ exists at $T_{c1} \simeq 220$ K. The composition dependence of the temperature $T_{c\chi}$ (T_{c1}) at which $|d\chi/dT|$ has a peak is shown in figure 6 by the full downward-pointing triangles. It should be noted that the composition with $x = 0.75$ has two transitions at T_{c1} and $T_{c3} \simeq 230$ K. For $x > 0.75$, very slight humps of χ seem to exist at T_{c3}, but it is not clear whether this result is inherent. At temperatures below T_{c1} and T_{c3}, the effective exchange coupling constants are expected to be smaller than those at high

Table 3. The susceptibility parameters of δ-$Ag_xV_2O_5$ at temperatures above 300 K; C is the Curie constant (emu K (mol V)$^{-1}$), T_W is the Weiss temperature (K) and χ_0 is the constant susceptibility (10^{-5} emu (mol V)$^{-1}$).

x	C	T_W	χ_0
0.650	0.123(2)	286(7)	2.2(1)
0.700	0.123(1)	217(4)	2.7(1)
0.725	0.127(1)	200(4)	2.0(1)
0.750	0.132(1)	179(4)	2.2(1)
0.775	0.133(2)	166(5)	2.2(1)
0.800	0.140(1)	170(2)	2.4(1)
0.850	0.139(5)	115(10)	0.5(3)

temperatures. There is no anomaly at T_{c2}, where $|\mathrm{d}\ln\rho/\mathrm{d}T^{-1}|$ and $|\mathrm{d}S/\mathrm{d}T^{-1}|$ for $x \geqslant x_c$ each have a peak.

The result for $x = 0.65$ at low temperatures may exhibit a spin gap having a significant decrease of the susceptibility with decreasing temperature. As described in section 2.2, the ground-state wavefunctions at the V1 and V2 sites in $Ag_{0.68}V_2O_5$ are both of d_{xy} type. Therefore, the superexchange couplings through the oxygen p orbitals between the V ions at a similar z-level in the ab-plane are expected to be most effective as regards magnetic properties. This consideration leads to the simplified spin network, the so-called trellis-layer model as shown in figure 4(c), where the thick lines and the broken lines denote[2] the corner-sharing V–V paths (J and J') and the edge-sharing one (J''), respectively. Recently, the magnetic susceptibility for this model with $S = \frac{1}{2}$ was calculated by quantum Monte Carlo simulations and the reduced fit function χ^* was presented [32]. Then, the susceptibility for $x = 0.65$ at temperatures below T_{c1} is described by the form

$$\chi = \frac{4C}{J_{\max}}\chi^* + \chi_{\mathrm{isolate}} + \chi_0 \tag{8}$$

where $J_{\max}$ is the largest exchange constant in the system and the second term is the Curie–Weiss-type susceptibility of the isolated V^{4+} ions with parameters of C_{isolate} and T_W^{isolate}. The full curve in figure 9(b) is drawn on the basis of the following parameters: $C = 0.106(1)$ emu K (mol V)$^{-1}$, $J = 46.9(5)$ K, $J' (= J_{\max}) = 193.4(6)$ K, $J'' = 108(1)$ K, $C_{\mathrm{isolate}} = 8.9(6) \times 10^{-4}$ emu K (mol V)$^{-1}$, $T_W^{\mathrm{isolate}} = 1.7(4)$ K and $\chi_0 = 2.9(2) \times 10^{-5}$ emu (mol V)$^{-1}$. The agreement between the experimental and calculated results is satisfactory. These parameters lead to the spin gap $\Delta = 140$ K and the Weiss temperature $T_W = 126$ K through the relation of

$$T_W = \frac{J}{2} + \frac{J'}{4} + \frac{J''}{2}.$$

This T_W is half of that estimated from the data at high temperatures above 300 K. Such a reduction of the exchange coupling constant has been seen above and below the spin-singlet transition temperature in NaV_2O_5 [13]. The compositions with $0.65 < x \leqslant 0.75$ with susceptibility maxima at low temperatures seem to remain paramagnetic. Therefore, nearly $\frac{1}{6}$-filling or commensurability of electrons ($x = \frac{2}{3}$ in this case) may be one of the origins for the spin-gap state of $Ag_{0.65}V_2O_5$, taking account of the EPMA result (figure 1).

The susceptibility result for $x = 0.80$ and 0.85 appears to exhibit a broad peak as expected for the low-dimensional spin system, although the low-temperature behaviour has a significant Curie tail. Considering that χ for $x = 0.85$ has the form

$$\chi = \chi_{1\mathrm{D}} + \chi_{\mathrm{isolate}} + \chi_0 \tag{9}$$

[2] The Heisenberg Hamiltonian is defined as $H = \sum_{\langle i,j\rangle} J\boldsymbol{S}_i \cdot \boldsymbol{S}_j$, where $\boldsymbol{S}_i$ is the spin operator at site i.

where the first term is the susceptibility for an $S = \frac{1}{2}$ antiferromagnetic Heisenberg-chain system with the Curie constant C_{1D} and the exchange constant J_{1D} [33], the data are almost explained as shown by the full curve in figure 9(b), where $C_{1D} = 0.125(1)$ emu K (mol V)$^{-1}$, $J_{1D} = 179(1)$ K, $C_{isolate} = 0.010$ emu K (mol V)$^{-1}$, $T_W = 4.4(1)$ K and $\chi_0 = 0.7(1) \times 10^{-5}$ emu (mol V)$^{-1}$. The total of C_{1D} and $C_{isolate}$ nearly corresponds to the value expected from the chemical formula. Considering that J_{1D} corresponds to J or J'' in figure 4(c), we obtain $T_W = 90$ K, which is close to the value estimated at high temperatures (table 3). This is consistent with the absence of a structural transition for this composition. It should be noted that this result is very similar to that for $Ca_{1-x}Na_xV_2O_5$ with $0.9 \leqslant x < 0.98$, where only J is effective [13]. Therefore, deviations from the Curie–Weiss law at low temperatures are attributed to the spin fluctuations in the linear-chain system.

3.4. Electron paramagnetic resonance

EPR measurements, for the sintered specimens of $Ag_xV_2O_5$ with $x = 0.65$, 0.70 and 0.90, were performed in the heating process at temperatures between 14 and 300 K at 9.2 GHz using a JEOL spectrometer.

For all of the specimens, the line shape is a single Lorentzian and the g-factor is nearly temperature independent, $g \simeq 1.96$, which corresponds to the values for Heisenberg magnets with the d_{xy}-type ground-state wavefunction [13]. The spin susceptibility extracted on the basis of the integration of the signal, taking account of the temperature dependence of a Q-factor, nearly corresponds to the behaviour shown in figures 9(a) and 9(b), which is consistent with the result that the static susceptibility comes from the V spins. The peak-to-peak linewidth of the absorption derivative, W, as a function of temperature is shown in figure 10. At high temperatures, W is nearly constant, and at low temperatures, it is linear in temperature. In the intermediate-temperature region, the result for $x = 0.65$ indicates an upturn at T_{c1}, and at a similar temperature, a slight hollow appears for $x = 0.70$. For $x = 0.90$, on the other hand, no anomaly exists there. These results are consistent with those described before. Since the anisotropy of the linewidth cannot be measured owing to the twinning of the crystalline specimens, it is difficult to consider the relaxation mechanism in detail. However, for the linear-chain system with $x = 0.90$ (section 3.3), it may be said that the Dzyaloshinsky–Moriya antisymmetric exchange interaction is the most probable mechanism. The space-averaged linewidth in the high-temperature limit due to this mechanism is about 10 mT, from the relation

$$\langle W_{DM} \rangle = 9^{-1}\sqrt{3}\,\Delta g^2\, g^{-3}\mu_B^{-1} J_{1D} \tag{10}$$

where $\Delta g = 2.0023 - g$ and μ_B is the Bohr magneton [13]. This magnitude is comparable to the experimental result.

4. Further discussion and conclusions

The structural and electronic properties of the δ-phase $Ag_xV_2O_5$ system with the single-phase region $0.65 \leqslant x \leqslant 0.90$ have been investigated in detail from multiple viewpoints.

The redetermined structure of $Ag_{0.68}V_2O_5$ indicates that two crystallographically independent V ions in the V_2O_5 double layers have valences close to the average value expected from the chemical formula. Since the superexchange coupling between the V ions at a similar z-level is considered to be most effective, judging from the crystal-field analysis, the trellis-layer model may be applied to this system. Disorder of the Ag ions is also found.

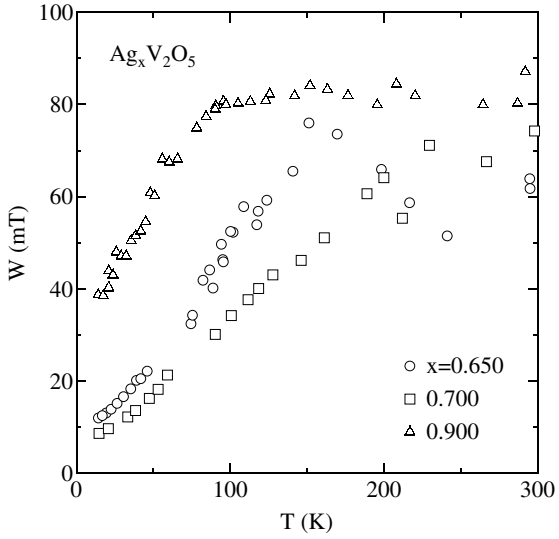

Figure 10. The temperature dependence of the EPR linewidth W of δ-$Ag_xV_2O_5$ in the heating process.

For the range $0.65 \leqslant x \leqslant 0.75$, first-order phase transitions with structural, transport and magnetic anomalies appear at $T_{c1} \simeq 220$ K, which decreases slightly with increasing x. At temperatures below T_{c1}, a nearly $\frac{1}{6}$-filled compound is in the spin-singlet state with an energy gap of 140 K and other compositions with characteristic susceptibility maxima seem to remain paramagnetic, where the superexchange coupling constant is significantly reduced as compared with that at high temperatures. In order to clarify whether the low-temperature state is gapless except for in the $\frac{1}{6}$-filling condition, another test is necessary. The phase at temperatures below T_{c1} may be accompanied by the ordering of Ag ions.

For $0.80 \leqslant x < 0.85$, the transition at T_{c1} disappears, and the only transport anomaly occurs at $T_{c2} \simeq 170$ K, this temperature decreasing slightly with increase of x. Here, the composition with $x = 0.85$ is excluded from this range, since only the resistivity result exhibits a slight anomaly, which is inconsistent with the thermoelectric power result, and is probably due to a slight inhomogeneity of the specimens. The transition at T_{c2} is probably caused by the nonperiodic Coulomb potential of Ag ions. The composition with $x_c \simeq 0.775$, at which the x-dependence of the lattice constants changes, corresponds to the point of crossover between the phases with T_{c1} and T_{c2}. At around x_c, an additional transition at $T_{c3} \simeq 230$ K appears, indicating the complex phase. For $0.85 \leqslant x \leqslant 0.90$, no anomaly exists there, since the random-potential effect of Ag ions would become smaller.

For $0.80 \leqslant x \leqslant 0.90$, the magnetic properties essentially exhibit linear-chain behaviours with a superexchange coupling constant of 180 K. The transport properties for $x \leqslant x_c$ and $x > x_c$ indicate negative and positive small-polaron conductions, respectively. The electronic state for the former composition range may be near to a variable-range hopping state originating from the random-potential effect of Ag ions. This is similar to the crossover of transport properties for the insulator side in the spinel-type $Li_{x\,p}Mg_{1-x}V_2O_4$ system with a metal–insulator transition.

In order to explain the linear-chain magnetic properties for $x \geqslant 0.80$, two models may be considered: (i) only the exchange coupling J is dominant; and (ii) only J'' is important.

Here, it has been postulated that the valences of V ions for this composition are distributed homogeneously. Considering that the transfer integral for the path corresponding to J' is not small, the former model should be applied with spins attached to the V–O–V molecular orbital for the path of J', where the ground state is the state with electrons localized in the bonding orbital as in the case of NaV_2O_5. In other words, the electronic state for this composition range may be characterized as the state with the freedom of the charge order at the local sites. From this viewpoint, the positive small-polaron conduction for $x > x_c$ may be regarded as being due to hole carriers in the quarter-filled Mott insulator of the virtual composition AgV_2O_5. On the other hand, for $x \leqslant 0.75$, spins are attached to a single V ion with the strong electron–phonon interaction, so J' is effective.

In δ-$Ag_xV_2O_5$, both the low dimensionality of the electronic state and the electron–phonon-coupling effect (ionic nature) may result in a small transfer integral or a small bandwidth. In addition, the random-potential effect of Ag ions produces varied properties. This work indicates an apparent crossover between the spin-gap state and the linear-chain state with the V–O–V molecular orbital. In order to further clarify the difference between these states, full structure determinations for the low-temperature phase with T_{c1} and for the highly Ag-doped compound are very necessary.

References

[1] Bouloux J-C and Galy J 1973 *Acta Crystallogr.* B **29** 1335
[2] Bouloux J-C and Galy J 1973 *Acta Crystallogr.* B **29** 269
[3] Onoda M and Nishiguchi N 1996 *J. Solid State Chem.* **127** 359
[4] Kodama K, Harashina H, Sasaki H, Kobayashi Y, Kasai M, Taniguchi S, Yasui Y, Sato M, Kakurai K, Mori T and Nishi M 1997 *J. Phys. Soc. Japan* **66** 793 and references therein
[5] Fukumoto Y and Oguchi A 1998 *J. Phys. Soc. Japan* **67** 2205 and references therein
[6] Onoda M and Ohyama A 1998 *J. Phys.: Condens. Matter* **10** 1229
[7] Harashina H, Kodama K, Shamoto S, Taniguchi S, Nishikawa T, Sato M, Kakurai K and Nishi M 1996 *J. Phys. Soc. Japan* **65** 1570
[8] Smolinski H, Gros C, Weber W, Peuchert U, Roth G, Weiden M and Geibel C 1998 *Phys. Rev. Lett.* **80** 5164
[9] Meetsma A, de Boer J L, Damascelli A and Palstra T T M 1998 *Acta Crystallogr.* C **54** 1558
[10] von Schnering H G, Grin Y, Kaupp M, Somer M, Kremer R K, Jepsen O, Chatterji T and Weiden M 1998 *Z. Kristallogr.—New Cryst. Struct.* **213** 246
[11] Horsch P and Mack F 1998 *Eur. Phys. J.* B **5** 367
[12] Isobe M and Ueda Y 1996 *J. Phys. Soc. Japan* **65** 1178
[13] Onoda M and Kagami T 1999 *J. Phys.: Condens. Matter* **11** 3475
[14] For example, Galy J 1992 *J. Solid State Chem.* **100** 229
[15] Onoda M and Nagasawa H 1987 *Phys. Status Solidi* b **141** 507 and references therein
[16] Andersson S 1965 *Acta Chem. Scand.* **19** 1371
[17] Casalot A and Pouchard M 1967 *Bull. Soc. Chim.* **10** 3817
[18] Casalot A, Cazemajor H, Hagenmuller P, Pouchard M and Roch J 1968 *Bull. Soc. Chim.* **1** 85
[19] Casalot A 1969 *Bull. Soc. Chim.* **4** 1103
[20] For example, Kawakita J, Sasaki H, Eguchi M, Miura T and Kishi T 1998 *J. Power Sources* **70** 28 and references therein
[21] Onoda M, Ohta H and Nagasawa H 1991 *Solid State Commun.* **79** 281
[22] Burla M C, Camalli M, Cascarano G, Giacovazzo C, Polidoli G, Spagna R and Viterbo D 1989 *J. Appl. Cryst.* **22** 389
[23] Cromer D T and Waber J T 1974 *International Tables for X-Ray Crystallography* vol 4, ed J A Ibers and W C Hamilton (Birmingham: Kynoch) section 2
[24] Creagh D C and McAuley W J 1992 *International Tables for Crystallography* vol C, ed A J C Wilson (Boston, MA: Kluwer Academic)
[25] teXsan 1992 *Crystal Structure Analysis Package* (The Woodlands, TX: Molecular Structure Corporation)
[26] Zachariasen W H 1978 *J. Less-Common Met.* **62** 1
[27] Freeman A J and Watson R E 1965 *Magnetism* part A vol 2 ed G T Rado and H Suhl (New York: Academic)

[28] Shannon R D 1976 *Acta Crystallogr.* A **32** 751
[29] Onoda M, Imai H, Amako Y and Nagasawa H 1997 *Phys. Rev.* B **56** 3760
[30] Onoda M and Kohno M 1998 *J. Phys.: Condens. Matter* **10** 1003
[31] Heikes R R 1961 *Thermoelectricity* ed R R Heikes and R W Ure (New York: Interscience)
[32] Johnston D C, Troyer M, Miyahara S, Lidsky D, Ueda K, Azuma M, Hiroi Z, Takano M, Isobe M, Ueda Y, Korotin M A, Anisimov V I, Mahajan A V and Miller L L 2000 *Preprint* cond-mat/0001147
[33] Bonner J C and Fisher M E 1964 *Phys. Rev.* **135** A640